

Contents lists available at ScienceDirect

# Applied Catalysis B: Environmental

journal homepage: www.elsevier.com/locate/apcatb



# Hierarchically porous Cu/Zn bimetallic catalysts for highly selective CO<sub>2</sub> electroreduction to liquid C<sub>2</sub> products



Xingsong Su<sup>a,b</sup>, Yuanmiao Sun<sup>d</sup>, Lei Jin<sup>b</sup>, Lei Zhang<sup>a,b</sup>, Yue Yang<sup>b</sup>, Peter Kerns<sup>b</sup>, Ben Liu<sup>a,\*</sup>, Shuzhou Li<sup>d,\*</sup>, Jie He<sup>b,c,\*\*</sup>

<sup>a</sup> Jiangsu Key Laboratory of New Power Batteries, Collaborative Innovation Center of Biomedical Functional Materials, School of Chemistry and Materials Science, Nanjing Normal University, Nanjing 210023, China <sup>b</sup> Department of Chemistry, Institute of Materials Science, University of Connecticut, Storrs, CT 06269, USA <sup>c</sup> Polymer Program, Institute of Materials Science, University of Connecticut, Storrs, CT 06269, USA <sup>d</sup> School of Materials Science and Engineering, Nanyang Technological University, Singapore 639798, Singapore

#### ARTICLEINFO

#### Keywords: Hierarchically porous materials Cu/Zn alloys Templated synthesis CO<sub>2</sub> electroreduction Selectivity

#### ABSTRACT

Hierarchically macroporous-mesoporous (HMMP) Cu/Zn alloy catalysts are reported to promote  $CO_2$  electroreduction towards liquid  $C_2$  products. HMMP Cu/Zn alloys with two types of distinct pores (~320 nm and ~20 nm) and adjustable alloy compositions are prepared through the interfacial self-assembly of two polymer templates and metal precursors. Due to add-in synergies of hierarchically porous structures and bimetallic elemental compositions, the resultant HMMP Cu/Zn alloy catalysts remarkably promote the deep electroreduction of  $CO_2$  to liquid  $C_2$  products while simultaneously suppressing the competitive proton reduction. Among them, HMMP  $Cu_3Zn_8$  exhibits the best electrocatalytic selectivity (with a very high ethanol production of 46.6 % at -0.8 V) and excellent stability (even after electrocatalysis for 11 h) towards  $CO_2$  electroreduction. This strategy allows for the reliable synthesis of other HMMP alloy nanocatalysts for a wide range of electrocatalytic applications.

# 1. Introduction

Effective capture and conversion of  $CO_2$  to produce valuable chemicals/fuels has received considerable attention as a means to reduce  $CO_2$  emissions and transform the world's energy system. Reducing  $CO_2$  involves multi-electron and multi-proton transfers that often bring a large kinetic barrier and a broad range of reduction products [1–4]. New catalysts are key for reducing  $CO_2$  efficiently and selectively. Among all synthetic catalysts developed for the electrocatalytic  $CO_2$  reduction in aqueous solution so far, only Cu-based electrocatalysts are capable of carrying out deep reduction of  $CO_2$  to  $C_2$  products. However, Cu electrocatalysts show a low Faradaic efficiency (FE) for  $CO_2$  reduction and  $C_2$  products (e.g., ethylene) selectivity [5,6]. Commercial Cu foil as an example only shows a FE of ca. 50 % toward  $CO_2$  reduction while competing with proton reduction, also known as hydrogen evolution reaction (HER) [7]. Although there is a tremendous amount of literatures on the fundamental understanding of the morphologies [8–13], nanostructures [13–19], surface crystal facets [20] of Cu catalysts on their activity and selectivity

towards  $CO_2$  reduction, selective  $CO_2$  electroreduction to liquid  $C_2$  products remains as an unmet challenge.

Ethanol and acetate as the main liquid  $C_2$  products from  $CO_2$  electroreduction are among the most desirable products [21–24]. Reducing  $CO_2$  to ethanol needs  $12e^-$  transfer and that to acetate needs  $8e^-$ . The essential step towards the formation of  $C_2$  products is the formation of CeC bond; that is, the coupling of the key intermediate \*CO occurs on the surface of CeC catalysts [6,25]. Desipt being most desirable, the deep reduction products, such as ethylene, ethanol and acetate [5,7,26–29], usually show low selectivity and yield during  $CO_2$  electroreduction. When optimizing the nanostructures of the CeC catalysts became more selective to produce ethylene up to 90 % [30,31]. Previous simulation results suggest that, the formation of the key intermediate \*CO on CeC is slow while the further conversion of \*CO through coupling and hydrogenation is kinetically favorable [28,32,33]. In view of new catalysts to effectively convert  $CO_2$  to  $C_2$  products, control of the surface composition to promote the formation of \*CO intermediates potentially play an important role

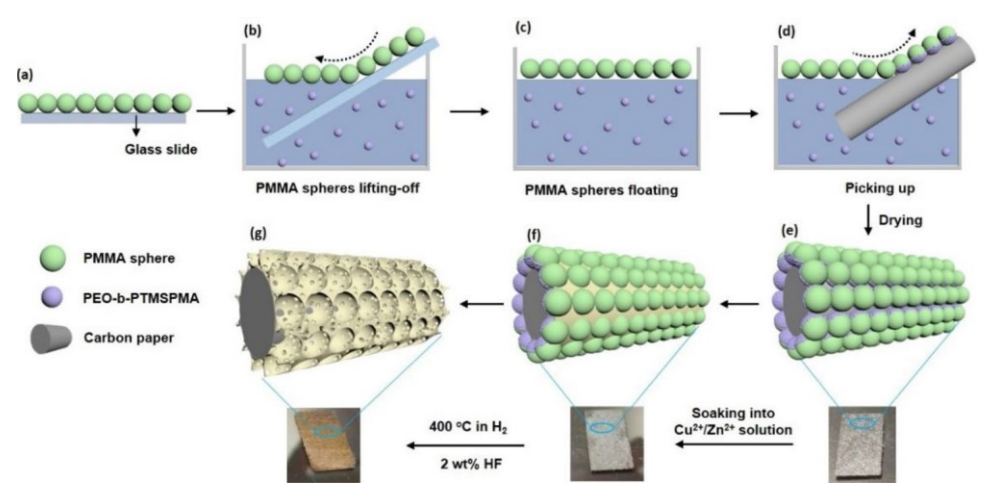
<sup>&</sup>lt;sup>®</sup> Corresponding authors.

Corresponding author at: Department of Chemistry, University of Connecticut, Storrs, CT 06269, USA. E-mail addresses: ben.liu@njnu.edu.cn (B. Liu), lisz@ntu.edu.sg (S. Li), jie.he@uconn.edu (J. He).

in tuning the activity and selectivity [34–36]. Unfortunately, the doping of Cu with Sn [37,38] and Au [39] that have been well-known to promote the formation of \*CO intermediates would lead to the loss of deep reduction products. This is due to the lack of the strong binding of \*CO intermediates to the doped Cu catalysts. On the other hand, Zn with a similar 3d electron configuration as Cu show activity for 2e<sup>-</sup> reduction of CO<sub>2</sub> to CO and formate [7,40,41]. When doping electron-rich Zn to Cu, Cu/Zn alloys show high activity for CO<sub>2</sub>, in particular with suppression of HERs and promote the formation of alcohol products [42,43]. For example, Cu<sub>4</sub>Zn has an FE of 29.1 % towards ethanol through promoting the formation of CeC bonds of the two neighboring C<sub>1</sub> intermediates on the surface of Cu [42]. When mixing Cu<sub>2</sub>O with ZnO (1: 0.5, wt), the hybrid catalysts enhanced the methanol formation at a rate of  $4.9 \times$ 10<sup>-5</sup> mol m<sup>-2</sup> s<sup>-1</sup> and the FE to methanol reached to 25.2 % at -1.3 V vs. Ag/AgCl, respectively. ZnO as a co-catalysts likely strengthens the bonding between Cu and CO- intermediate, resulting in a large increase of CO<sub>2</sub> reduction selectivity to alcohols [44].

Cu/Zn alloys were usually prepared through electrodeposition or electroreduction [42]. Since the reduction potentials of  $\mathrm{Cu}^{2+}$  and  $\mathrm{Zn}^{2+}$  are largely different  $^{E}_{Z_{n}Z^{2+}/n} = -0.76$  V and  $^{E}_{Cu}_{C^{2+}/u} = 0.34$  V (vs. reversible hydrogen electrode, RHE, all potentials reported here are with respect to RHE), it is difficult to synthesize bimetallic  $\mathrm{Cu}/\mathrm{Zn}$  alloys which are extremely critical to tune their electrocatalytic activity and product selectivity.

Another important factor to control the product selectivity toward  $CO_2$  reduction is the retention time of intermediates. Since the formation of deep reduction products is kinetically unfavorable, the design of nanocatalysts to prolong the interaction of intermediates with catalysts can significantly promote the formation of  $C_2$  products [9,45–49]. Among many other nanostructures, porous materials are of particular interest to not only increase the surface-to-



volume ratios and active sites on the surface, but also to control the localized pH within the pores and the mass transport of the reactants/intermediates/products with its defined pore structures [46,50]. Nam and co-workers demonstrated that the pore size of mesoporous Cu catalysts is important to control the selectivity of  $C_2$  products [9]. When decreasing the pore size from 300 to 30 nm, the FE of ethylene was enhanced from 8% to 38 %. Similar morphological effects have been shown in Au and  $SnO_2$  catalysts for  $CO_2$  reduction as well [48,49].

We herein report the wet-chemical synthesis of porous bimetallic Cu/Zn catalysts for selective CO<sub>2</sub> electroreduction to liquid C<sub>2</sub> products. The synthesis of the bimetallic catalysts is based on an interfacial selfassembly method of two polymer nanospheres having different sizes as templates (see Scheme 1). Ordered and closely packed polymer templates were fabricated on the surface of a hydrophilic carbon paper electrode first; then physically adsorbed Cu<sup>2+</sup> and Zn<sup>2+</sup> ions through electrostatic interaction and coordination with the two polymer templates. The formation of uniform bimetallic Cu/Zn catalysts was achieved by high-temperature reduction using hydrogen, therefore affording

uniform distribution of the two metals with highly surface areas and defined crystalline structures. Our method allows tuning the alloy composition by simply varying the ratios of metal precursors. Hierarchically macroporous-mesoporous (HMMP) Cu/Zn alloys have macropores of ~320 nm and mesopores of ~20 nm. We found that the doping of Zn to Cu largely promotes the formation of \*CO intermediates to weakly cover the surface of Cu. This in turn results in the increase of the energy barrier to reduce protons and improves the overall FE toward  $\rm CO_2$  reduction. Hierarchical porosity of the bimetallic catalysts largely enhanced the retention time of intermediates to promote the deep reduction of  $\rm CO_2$  to form liquid products. The porous  $\rm Cu_5Zn_8$  catalyst shows a FE toward liquid  $\rm C_2$  products (ethanol and acetate) of 58.3 % at -0.8 V with a specific current density ( $J_{CO2}$ ) of 3.6 mA/cm² under steady-state electrolysis for 11 h.

#### 2. Results and discussion

To prepare HMMP Cu/Zn alloyed films, hydrophobic PMMA nanospheres (an average dimeter, ~350 nm) and polymer micelles of poly (ethylene oxide)<sub>114</sub>-block-poly(3-(trimethoxysilyl)propy methacrylate)<sub>298</sub> (PEO<sub>114</sub>-b-PTMSPMA<sub>298</sub>, with average dimeter of ~23 nm) were used as the templates for macropores and mesopores, respectively (Fig. S1-2, see synthetic details in SI). In brief, a monolayer of ordered and close-packed PMMA nanosphere array was prepared on a clean glass slide driven by surface tension at the interface of water/glass/air (Scheme 1a) [51,52]. The PMMA array was then transferred and lifted off on the top of an aqueous solution containing polymer micelles (15 mg/mL). The array can float at the water-air interface due to the hydrophobic nature of PMMA nanospheres (Scheme 1b and c). The monolayer of the PMMA nanospheres was then picked up using a carbon paper electrode. During the

transfer, the interfacial self-assembly of polymer micelles occurred within the PMMA array to fill the voids in between larger PMMA nanospheres (Scheme 1d). After drying at 80 °C for overnight, the same procedure was repeated twice to form the three layers of PMMA nanospheres. After coated with the two templates, the carbon paper electrode was then immersed into the aqueous solution containing metal precursors, e.g., Cu(NO<sub>3</sub>)<sub>2</sub> and Zn (NO<sub>3</sub>)<sub>2</sub>. The alloy composition can be varied by tuning the Cu/Zn molar ratio. After soaking with metal precursors, the carbon paper electrode was further calcined under H2 at 400 °C to reduce Cu and Zn ions and remove the PMMA templates (Scheme 1f). The formation of Cu and Cu/Zn alloys on the carbon paper electrode is obvious

as the color of the carbon paper electrode became golden after calcination. In the course of calcination, polymer micelles evolved into solid silica nanoparticles to support the metallic framework [53–55]. Finally, silica residues were

Scheme 1. Schematic illustrating the synthetic strategy of HMMP Cu/Zn alloyed catalysts on a carbon paper through the interfacial self-assembly method. The pictures on the bottom show the Cu/Zn alloy on carbon paper, the templates with metal precursors on the carbon paper and the templates on carbon paper without metal precursors (from left to right). etched to release the mesopores by 2 wt% hydrofluoric acid (HF) (Scheme 1g). To confirm the thickness, the HMMP Cu/Zn alloy was also fabricated on a silicon wafer to image the cross-section.

XRD peaks appeared for alloyed catalysts, suggesting the formation of pure alloys.

Since Zn atoms are slightly smaller than that of Cu atoms, the incorporation of Zn into Cu resulted in the lattice contraction of Cu [60–62]. Amongst them, the (111) and (200) planes of Cu<sub>3</sub>Zn and CuZn are shown in Fig. 2b and c, respectively, both of which matched well to fcc Cu<sub>3</sub>Zn (JCPDS 03-6567) and

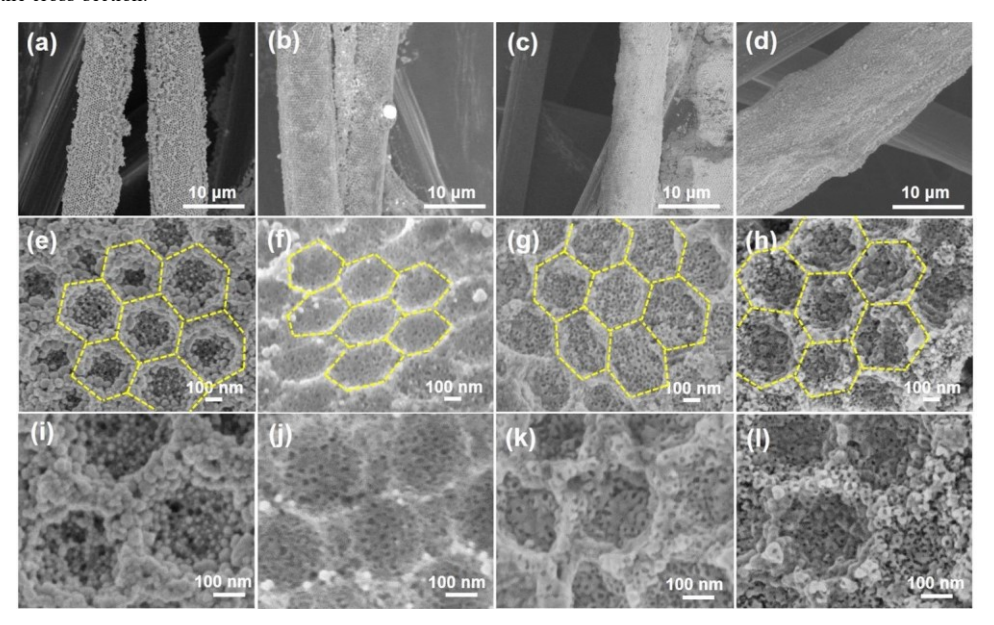


Fig. 1. Morphological characterizations of HMMP Cu/Zn alloyed catalysts with different compositional ratios. (a-d) Low and (e-l) high-magnification SEM images of monometallic Cu (a, e, i), bimetallic Cu<sub>3</sub>Zn (b, f, j), CuZn (c, g, k), and Cu<sub>5</sub>Zn<sub>8</sub>(d, h, l).

The nanostructures of as-prepared Cu/Zn alloys on the carbon paper electrode were first characterized by electron microscopy. As shown in scanning electron microscopy (SEM) (Fig. 1a-d), the carbon papers were uniformly coated by the Cu/Zn alloyed films. The alloyed film only appeared on the top surface of the carbon fibers. The average thickness of the Cu/Zn alloyed films is about 1 µm, as evidenced by the tri-layer film fabricated on the silicon wafer (Fig. S3), closely matching with the height of the three layers of PMMA nanospheres. HMMP features of Cu/Zn alloys were further revealed under higher magnifications. The Cu/Zn alloy films were interconnected by hexagonal closepacked macropores (Fig. 1e-h). The diameter of macropores estimated from the SEM images (Fig. 1e-h) is ~320 nm, slightly smaller than the diameter of PMMA nanospheres. This is due to the volume shrinkage of the PMMA templates during the thermal annealing [51]. The small angle X-ray scattering of the Cu<sub>5</sub>Zn<sub>8</sub> catalyst shows well-resolved (100) and (110) reflections, confirming an ordered hexagonal close packed mesostructure (Fig. S4a). The mesopores show homogenously dispersion in the framework of macropores as the hierarchically porous framework of the alloyed films. This is observed clearly by transmission electron microscopy (TEM) (Fig. S4b-d). Mesopores are fairly spherical with an average diameter of 20 nm (Fig. 1j-1, S4a and Table S1). Furthermore, the density of mesopores in the alloyed films with a higher ratio of Zn, e.g., CuZn and Cu<sub>5</sub>Zn<sub>8</sub>, is higher than that in pure Cu and Cu<sub>3</sub>Zn with a lower Zn ratio. One noticeable change is the size of the crystalline grains which is much smaller in pure Cu and Cu<sub>3</sub>Zn, compared to the other two alloys (Fig. 1e and i). This is likely because of the increase in the thermoplasticity of Cu-based alloy with the increase of Zn amount in alloys, further leading to the formation of the stable mesopores structures [56,57].

Crystallinity and surface compositions of HMMP Cu/Zn alloys were examined by wide-angle X-ray diffraction (XRD) and SEM energy-dispersive X-ray spectroscopy (EDS) mappings. As shown in Fig. 2a, the diffraction peaks at 43.3°, 50.4° and 74.0° for pure Cu film are ascribed to (111), (200) and (220) planes, respectively, indicating the metallic face-centered cubic (fcc) Cu phase (JCPDS 03-1005). After alloyed with Zn, all peaks shifted to a lower 20 [58,59]. The diffraction patterns of Cu/Zn alloys are similar to that of pure Cu. No new

body-centered cubic CuZn (JCPDS 060657). Noticeably, a slightly different XRD pattern was observed for  $Cu_5Zn_8$ , known as a complex cubic phase. High-resolution TEM image shows that the lattice fringes correspond to a d-spacing of 0.112, 0.184 and 0.214 nm, which match well with the d-spacing of the (214), (202) and (012) planes of the  $Cu_5Zn_8$  alloy, respectively (Fig. S4c). Those results confirm the successful preparation of HMMP Cu/Zn alloyed catalysts with rationally adjustable compositions and also highlight the versatility of our synthetic method for bimetallic Cu/Zn alloys. Ideally, our fabrication method is capable of synthesizing Cu/Zn alloys with any Cu/Zn ratios which is not possible through solution synthesis or electrochemical co-reduction.

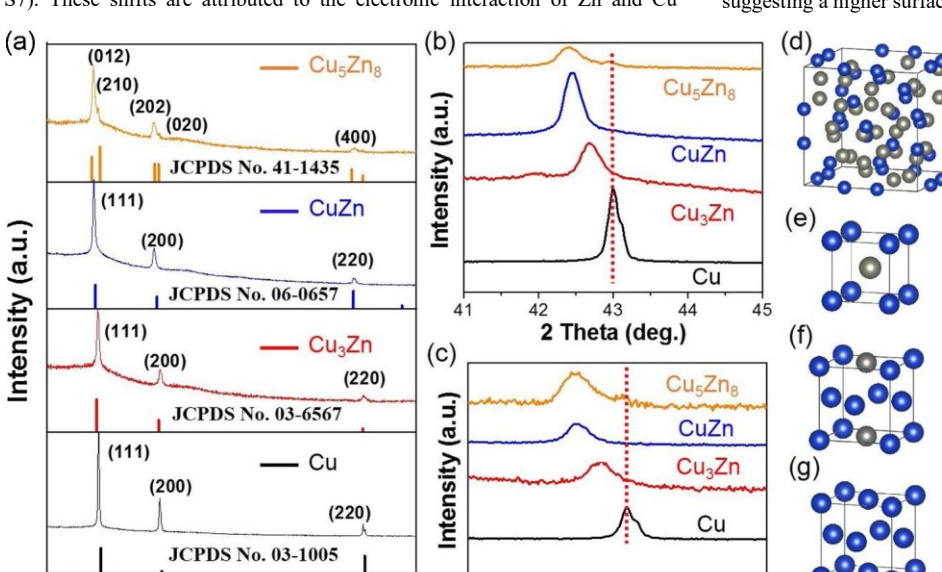
The compositions of bimetallic Cu/Zn alloys were estimated using SEM-EDS mappings. Those results are summarized in Fig. S5. A homogeneous distribution of Cu and Zn throughout was seen for all CuZn alloyed films. The atomic ratio of Cu-to-Zn on Cu<sub>3</sub>Zn, CuZn and Cu<sub>5</sub>Zn<sub>8</sub> was measured to be 1.0 : 0.2, 1.0 : 1.2 and 1.0 :1.8, close to the molar ratio of Cu to Zn in the solution (1.0 : 0.3, 1.0 : 1.0 and 1.0 : 3.0), respectively. This observation indicates the stoichiometric ratio of the HMMP alloys can be easily controlled by the feeding ratio. The surface compositions of Cu and Zn were also evaluated using X-ray photoelectron spectroscopy (XPS). The ratios of elements on the surface of HMMP Cu<sub>3</sub>Zn, CuZn and Cu<sub>5</sub>Zn<sub>8</sub> alloys were 1.0 : 0.5, 1.0 : 1.1 and 1.0 : 3.5, respectively (see Fig. S6), indicating slightly more Zn on the surface of the alloys. This is attributed to the surface oxidation of Zn to form ZnO (~7%) as confirmed by Zn and Cu LMM Auger analysis on Cu<sub>5</sub>Zn<sub>8</sub> alloy (Fig. S6e).

40

50

60

High-resolution XPS was used to compare the surface electronic states of bimetallic Cu/Zn alloyed catalysts and further understand the charge interaction between Cu and Zn (see Fig. S7). The pure Cu film shows the two Cu 2p peaks, including Cu  $2p_{1/2}$  and Cu  $2p_{3/2}$  at 952.5 eV and 932.6 eV, respectively. A gradual decrease in Cu 2p binding energy was observed when alloying with Zn. The Cu  $2p_{3/2}$  peak shifted to 932.5 eV for Cu<sub>3</sub>Zn, 932.5 eV for CuZn and 932.4 eV for Cu<sub>5</sub>Zn<sub>8</sub>. On the other hand, Zn  $2p_{3/2}$  shifted to slightly higher binding energies when increasing the Zn content in the bimetallic Cu/Zn alloys (see Fig. S7). These shifts are attributed to the electronic interaction of Zn and Cu



indicative of the weakened adsorption of \*CO intermediates [70]. The formation of intermediates was measured using the attenuated total reflectance surface-enhanced infrared spectroscopy (ATRSEIRAS). Using Cu<sub>5</sub>Zn<sub>8</sub> catalysts at -0.7 V, \*COOH and \*CO as key intermediates were observed (Fig. S9). It is reasonable since Zn is known to be less favorable for CO binding from previous literatures [71]. A higher Zn content in the bimetallic catalysts results in weakly adsorbed \*CO species, which show a lower reduction potential. On the other hand, the peak current of \*CO reduction is enhanced at a higher Zn content, suggesting a higher surface coverage of adsorbed \*CO species on the catalysts.

Fig. 2. Structural characterizations of HMMP Cu/Zn catalysts with different compositional ratios. (a) Wide-angle XRD patterns and zoomin XRD patterns in the range of (b)  $41^{\circ}$  –  $45^{\circ}$  and (c)  $48^{\circ}$  –  $52^{\circ}$  of the Cu/Zn alloyed films. Schematic illustrations of the crystal structures for (d) Cu<sub>5</sub>Zn<sub>8</sub> (complex cubic), (e) Cu/Zn

(body-centered cubic), (f)  $Cu_3Zn$  (face-centered cubic) and (g) pure Cu (face-centered cubic).

2 Theta (deg.)
because of the larger work function of Cu than that of Zn (the work function of pure Cu and Zn is 4.7 and 4.3, respectively) [39,60,63]. The lowering of the Cu 2p binding energy suggests that, i) the electron-rich Cu is present in all Cu/Zn alloys; and ii) Cu shows a higher electron density when increasing the Zn ratio in Cu/Zn alloys. The enhancement in surface electron density would lead to a lower d-band center of Cu, possibly weaken the chemisorption energy of some intermediates, e.g., CO [62,64,65].

80 48

The catalytic activity of the HMMP Cu/Zn alloys and the pure HMMP Cu film for CO<sub>2</sub> reduction was evaluated using an "H" cell separated with a Nafion proton exchange membrane. The working electrode and the reference electrode (a saturated calomel electrode) were sealed in one cylinder and the counter electrode (a graphite electrode) was in the other cylinder. The linear sweep voltammetry (LSV) of the catalysts was measured in N2 and CO2 saturated 0.1 M KHCO<sub>3</sub> aqueous solution using a three electrodes setup. The current density was normalized to the geometrical surface area of the carbon paper electrode, ca. 1 cm<sup>2</sup>. The LSV scans of the HMMP Cu<sub>5</sub>Zn<sub>8</sub> catalysts are displayed in Fig. 3a. Under CO<sub>2</sub>, the current density of the Cu<sub>5</sub>Zn<sub>8</sub> catalyst is significantly higher than that under N<sub>2</sub> atmosphere solution over the whole potential range. It is indicative of favorable CO<sub>2</sub> reduction over water reduction. As controls, the LSV curves of the carbon paper electrode and the commercial Cu foil were examined. The carbon paper shows negligible activity; while the commercial Cu foil is much less active in terms of its overpotential to reduce CO<sub>2</sub>. With the increase of the Zn content in the HMMP Cu/Zn alloys, the current density of the catalysts increased (Fig. S8).

A reduction peak on the LSV of  $\text{Cu}_5\text{Z}n_8$  was seen at -0.7 V vs RHE in  $\text{CO}_2$ -saturated solution [66,67]. This peak can be assigned to the reduction of the adsorbed \*CO intermediates on the electrode [68,69]. It is noteworthy that the potential and the current density of the peak is largely dependent on the ratio of Zn in the HMMP Cu/Zn alloys. The reduction peak of the HMMP pure Cu,  $\text{Cu}_3\text{Z}n$ , CuZn and  $\text{Cu}_5\text{Z}n_8$  catalysts appears at -0.53 V, -0.6 V, -0.66 V and -0.7 V, respectively (Fig. S8); while, the peak current increases with the ratio of Zn. In case of the pure Cu catalyst, this peak is barely noticeable. For the adsorbed species on the electrode, the gradual decrease in the reduction potential is

It implies that the presence of Zn in the bimetallic catalysts promotes the reduction of  $CO_2$  to \*CO intermediates. Interestingly to note, the increase of Zn content in the bimetallic catalysts results suppressed the HER. For example, the  $H_2$  FE of for the HMMP  $Cu_3Zn_8$  catalyst decreased to 11.8 % at its onset potential for  $CO_2$  reduction, while that of the pure Cu is close to 53 % (Fig. S10). This is likely due to the adsorbed CO intermediates preventing the competing adsorption of protons, therefore HER reactions simultaneously [68].

In order to unveil the origins of accelerated initial kinetics of  $CO_2$  reduction activity on various Cu/Zn alloys, density functional theory (DFT) calculations were used to investigate the intrinsic electronic properties of pure Cu,  $Cu_3Zn$ , CuZn, and  $Cu_5Zn_8$ , which have same compositions as experiments. The surface electron density of those catalysts in  $CO_2$  electroreduction is important to bind the reactants, which dominates the initial kinetics to some extent. Theoretically, the work function of the catalyst surface, defined as the thermodynamic energy to move an electron at the Fermi level to the vacuum outside the solid surface, is directly correlated to the initial binding. The calculated work function of the most stable surface of the four materials is summarized in Fig. 3b. Pure Cu exhibits the highest work function of 4.55 eV. When incorporated with Zn, the work function of bimetallic alloys gradually decreases to 4.50 eV, 4.46 eV, and 4.16 eV of  $Cu_3Zn$ , CuZn, and  $Cu_3Zn_8$  (Fig. 3b), respectively. This implies the enrichment of electrons and lowering the energy barrier to bind the electrophilic  $CO_2$ , which potentially accelerate binding kinetics of  $CO_2$ .

The computation of projected d-orbital density of states (DOS) of surface Cu atom was also performed to evaluate the trend observed on the bimetallic catalysts. As proposed by Norskov and co-workers [71], the d-band center provides intrinsic electronic information to explain the adsorption behavior of atomic species at the surface. The higher the d-band center, the stronger the chemisorption. Incorporating Cu with Zn dramatically changes the shape of the d-orbital structure of the surface Cu (Fig. 3c), thus alters the position of the d-band center. The pure Cu shows a d-band center of -2.12 eV, meaning it is highly active in adsorbing hydrogen atom. Comparatively, d-band center was calculated to be -2.32 eV, -2.43 eV, and -2.54 eV for Cu<sub>3</sub>Zn, CuZn, and

52

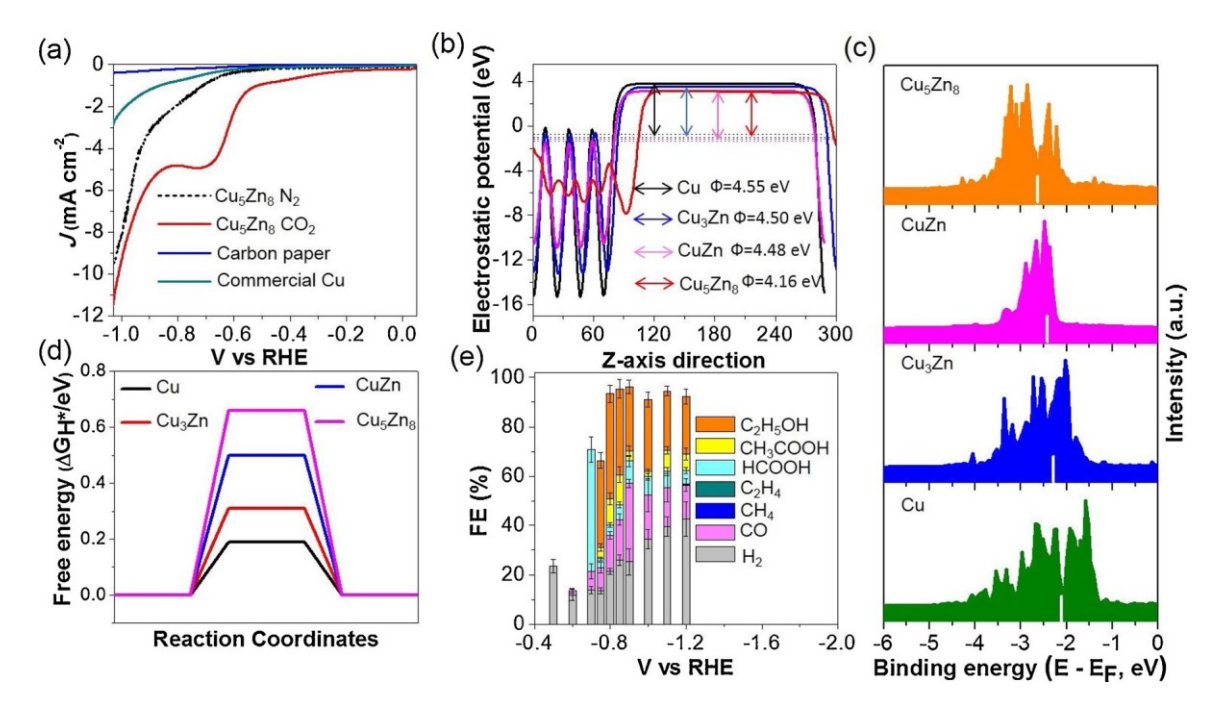


Fig. 3. (a) LSV curves of the HMMP  $Cu_5Zn_8$  catalysts at  $CO_2$  or  $N_2$ -saturated 0.1 M KHCO<sub>3</sub> solution, the uncoated carbon paper electrode and the commercial  $Cu_3$  foil at  $CO_2$ -saturated 0.1 M KHCO<sub>3</sub> solution. (b) Calculated electrostatic potentials and work functions of  $Cu_3Zn_3$ ,  $Cu_3Zn_4$ ,  $Cu_3Zn_5$ . The work function is defined as the energy needed to remove an electron from the solid catalyst to the vacuum level. (c) d-band center of the surface  $Cu_3Zn_4$ ,  $Cu_3Zn_5$ ,  $Cu_3Zn_5$ ,  $Cu_3Zn_6$ ,  $Cu_3Zn_8$ . (d) Calculated hydrogen adsorption free energy ( $\Delta Cu_3Zn_4$ ) on  $Cu_3Zn_5$ ,  $Cu_3Zn_5$ ,  $Cu_3Zn_6$ ,  $Cu_3Zn_8$ . (e) FE of major products vs. potential for the HMMP  $Cu_3Zn_8$  catalyst at a

Cu<sub>5</sub>Zn<sub>8</sub>, respectively. The binding affinity towards hydrogen gradually decreases as the Zn incorporation ratio increases, which corresponds to the trend observed on HER. It should be mentioned that the calculated d-band center also implies an increased trend in the co-adsorption energy of \*CO and \*CH<sub>2</sub> with the increase of Zn content. However, since the 12 elementary steps of CO<sub>2</sub> reduction to ethanol could bring a large variety of possible reaction pathways [72], it is difficult to evaluate whether this trend plays positive or negative role to the CO<sub>2</sub> reduction performance, as the co-adsorption of \*CO and \*CH<sub>2</sub> could be either an adsorption-limited or a desorption-limited step.

potential range of -0.5 V to -1.2 V in 0.1 M KHCO<sub>3</sub>.

Since CO2 and proton reductions (or HER) compete with each other, theoretical HER performance is analyzed by the hydrogen adsorption free energy ( $\Delta G_{H^*}$ ), with the optimal value staying at zero [73]. Thermodynamically, if ΔG<sub>H\*</sub> is too positive, it would be extremely difficult for the proton to be adsorbed on the catalyst surface and thus no reaction could take place; while if ΔG<sub>H\*</sub> is too negative, the surface of the catalyst would be easily occupied by proton and thus be less selective for CO<sub>2</sub>. Therefore, numerically, the farther the  $\Delta G_{H^*}$  away from zero value, the poorer the HER activity, and thus improved FE for CO<sub>2</sub> reduction. As shown in Fig. 3d, among the four candidates, pure Cu displays the best HER performance, with  $\Delta G_{H^*}$  calculated to be 0.19 eV. On the other hand, all the studied three Cu-Zn bimetallic systems show suppressed HER than pure Cu, with the higher Zn incorporation ratio contributing to poorer activity. Specifically, the value of ΔG<sub>H\*</sub> on Cu<sub>3</sub>Zn, CuZn, and Cu<sub>5</sub>Zn<sub>8</sub> evolves to be 0.31 eV, 0.50 eV, and 0.66 eV, respectively. Considering that 0.66 eV indicates a quite inert nature for catalyzing HER, Cu<sub>5</sub>Zn<sub>8</sub> shows significant advantage in improving CO<sub>2</sub> reduction efficiency.

To analyze the reduction product of  $\mathrm{CO_2}$  and gain insight into the selectivity of the HMMP alloys catalysts, the steady-state electrolysis was conducted at different potentials from -0.5 to -1.6 V vs RHE. At each potential,  $\mathrm{CO_2}$  reduction reaction was conducted to reach a total electric charge of 2–4 C. The gas sample was analyzed on a Shimadzu gas chromatography (GC) equipped with a thermal conductivity detector. The amount of gas products was obtained using the peak area of various gases based on the standard calibration curves. The liquid products were determined by using proton nuclear magnetic resonance with 1

mM dimethyl sulfoxide (DMSO) as an internal standard. The product analysis was carried out at least three times to calculate the standard deviation. The detailed analysis of gas and liquid products is given in SI and Figs. S10-S18. For the HMMP Cu<sub>5</sub>Zn<sub>8</sub> catalyst, up to 7 reduction products can be detected and their total FE adds up to 70-100 % (Tables S2-S5). CO as a product can be detected at an onset potential of -0.5 V. Since the current density is low at -0.5 V, only a small amount of H<sub>2</sub> and CO could be detected (Fig. 3e). When running at a more negatively potential (-0.7 V vs RHE), the conversion of CO<sub>2</sub> to CO and HCOOH was observed. The HCOOH FE of 49.4 % was achieved and the H<sub>2</sub>FE of less than 15 % was also observed. When further lowering the reduction potential, ethanol was produced as the main product, along with other products such as H<sub>2</sub>, CO, CH<sub>3</sub>COOH and HCOOH. At -0.8 V, the ethanol FE reaches 46.6 % with a specific current density of 2.3 mA/cm<sup>2</sup>. When considering the two liquid C2 products (ethanol and acetate), the FE toward C2 formation is 58.3 %. When further increasing the reductive potential, the ethanol FE deceased due to the competition with the HER.

In addition, the thickness of catalysts shows a strong impact on the selectivity of  $CO_2$  reduction. For example, single layered HMMP Cu shows a  $H_2$  FE of >65% and formate as the main  $CO_2$  reduction product at -1.2 V (Figs. S19 and S20a). When increasing to three layers of Cu, the  $H_2$  FE decreased to 49% while ethanol was produced with a FE of 9% at -1.2 V. This suggests that hierarchically porous catalysts can improve the deep reduction of  $CO_2$  and enhance the formation of  $CO_2$  products. This may be attributed to, i) the increased retention time of \*CO intermediates in the hierarchically porous CuZn catalysts, similar to the literatures [31,46–48]; and ii) Zn can strengthen the CU-\*CO link, resulting in an increase in the selectivity to alcohols as reported as reported previously [44,74].

The durability of the HMMP  $Cu_5Zn_8$  catalyst was examined using chronoamperometric (i-t) scan at -0.8 V vs RHE under a continuous flow of  $CO_2(Fig. 4a)$ . The HMMP  $Cu_5Zn_8$  catalyst shows a stable current of 4.3 mA/cm<sup>2</sup> during a continuous 11 h electrolytic  $CO_2$  reduction reaction. Although the FE

45.6 % at -0.8 V. At a lower potential, the conversion of CO<sub>2</sub> to ethanol increased significantly. The FE of ethanol reaches 35.7 % at -1.6 V for Cu<sub>3</sub>Zn (Fig. S20c). This trend becomes more obvious for the CuZn catalyst. The FE of ethanol is 34.6 % at -0.8 V (Figs. 4c and S20d). Similar to that of the HMMP

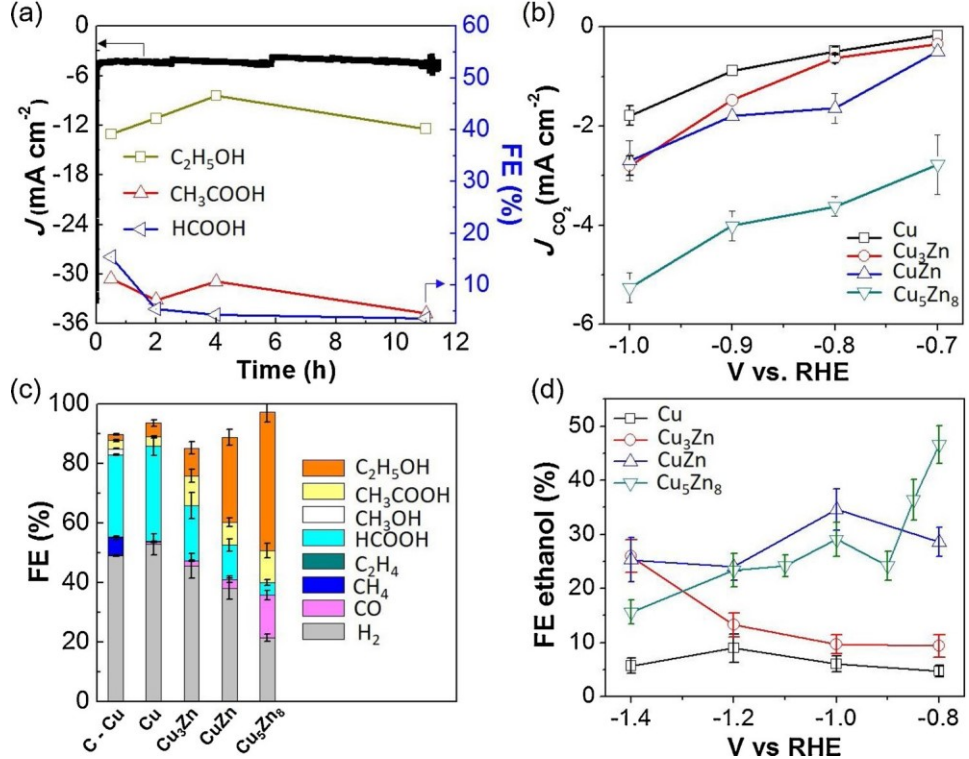


Fig. 4. (a) Stability test of the HMMP Cu<sub>5</sub>Zn<sub>8</sub> catalyst for 11 h. Left y-axis: the current density (J) of the HMMP Cu<sub>5</sub>Zn<sub>8</sub> catalyst at -0.8 V. Right y-axis: the FE of ethanol), EF (HCOOH) and FE (CH<sub>3</sub>COOH). (b) Partial current density (J) of total CO<sub>2</sub>. (c) Faradaic efficiency of H<sub>2</sub>,

CO, CH<sub>4</sub>, C<sub>2</sub>H<sub>4</sub>, HCOOH, CH<sub>3</sub>COOH and C<sub>2</sub>H<sub>5</sub>OH during electrochemical reduction of CO<sub>2</sub> on commercial Cu foil (C-Cu), HMMP pure Cu (H-Cu), Cu<sub>3</sub>Zn, CuZn and Cu<sub>5</sub>Zn<sub>8</sub> catalysts at -0.8 V vs RHE in 0.1 M KHCO<sub>3</sub>. (d) The FE of ethanol for the HMMP catalysts in the potential range of -0.8 to -1.4 V.

of liquid productions slightly decreases after 4 h, the FEs of ethanol and acetate were maintained at ~42 % and ~5% throughout the whole electrocatalytic process, respectively (Figs. 4a and S21). These results confirm that the Cu<sub>5</sub>Zn<sub>8</sub> catalyst shows an excellent stability. The morphology and the crystal structure of the Cu<sub>5</sub>Zn<sub>8</sub> catalyst before and after the CO<sub>2</sub> reduction reaction at ~0.8 V vs RHE were investigated using SEM and XRD (Figs. S22 and S23). There were cracks on the surface of the Cu<sub>5</sub>Zn<sub>8</sub> catalyst after 11 h of the CO<sub>2</sub> reduction reaction, but the macro/mesoporous and the crystallinity of the Cu<sub>5</sub>Zn<sub>8</sub> catalyst remained unchanged after electrolysis. The high stability of Cu<sub>5</sub>Zn<sub>8</sub> is likely attributed to the surface ZnO layer that prevents the agglomeration of the catalyst during electrolysis [44,75].

The current density toward  $CO_2$  reduction was used to assess the  $CO_2$  selectivity of the HMMP catalysts with different Cu/Zn compositions (Fig. 4b). The  $CO_2$  current density of  $Cu_5Zn_8$  is significantly higher than that of other catalysts, indicating that it is the most efficient to covert  $CO_2$  into the valuable products. This result is consistent with the surface CO coverage from LSV scans and the DFT calculation as described before. The  $Cu_5Zn_8$  alloy effectively inhibits hydrogen production; and  $J_{CO2}$  can reach 2.5 mA/cm² in a broad potential window from -0.7 V to -1.0 V. For a better comparison, the formation rate of ethanol based on the electrochemical surface area (ECSA) was calculated by double-layer capacitance method (Table S6). We have compared our results (e.g. formation rate, FE and current density of ethanol) with some recently reported Cu bimetallic catalysts as listed in Table S7 [5,42,74,76]. The HMMP  $Cu_5Zn_8$  catalyst outperformed the reported catalysts in terms of its activity and formation rate, as well as its selectivity for liquid  $C_2$  products, for  $CO_2$  reduction.

The product selectivity is highly determined by the composition of the HMMP Cu/Zn alloys. For the HMMP pure Cu,  $H_2$  and HCOOH are the major product; and the selectivity toward  $H_2$  and HCOOH is less potential-dependent. The FE of pure Cu to  $H_2$  and HCOOH is about 52.9 % and 32 % at -0.8 V, respectively (Figs. 4b and S20b). Similarly, for the HMMP  $Cu_3Zn$  catalyst, the formation of  $H_2$  and HCOOH is still dominant at its on-set potential. After the adding of Zn in Cu, the FE of  $H_2$  is slightly lower than that of pure Cu, e.g.,

Cu<sub>3</sub>Zn<sub>8</sub> catalyst, the selectively towards ethanol using the Cu/Zn alloy is dependent on the potential in comparison with pure Cu and Cu<sub>3</sub>Zn. At a lower potential that is far away from the reduction peak of \*CO intermediates, The FE of ethanol decreases dramatically. Interesting to note that, neither Cu nor Zn has been shown selectivity towards ethanol and acetate. For example, using pure Zn as the catalyst, CO is the favorable product with a FE > 80 % in recent literatures (Table S8) [42,77–84]; while, pure Cu is known to reduce CO<sub>2</sub> to methane and ethylene [26]. In the form of bimetallic Cu/Zn, the FE of the C<sub>2</sub> products (including ethanol and acetate) significantly increased up to 58 % and the selectivity to ethanol goes up to 46.6 % for the Cu<sub>5</sub>Zn<sub>8</sub> catalyst (Fig. 4d). Those findings suggest the profound catalytic synergies between Cu and Zn for CO<sub>2</sub> reduction [42,85].

The key step to promote the conversion of CO<sub>2</sub> to ethanol is the formation of the CeC bond, e.g., \*CO-CHO and \*CO-CH<sub>2</sub> [42]. The evolution of CO<sub>2</sub> to ethanol requires 12 proton-electron transfers and contains a large number of reaction intermediates. Among them, the coadsorption of two carbon-based intermediates is crucial, since the collision of two adsorbed C<sub>1</sub> species is essential to generate C<sub>2</sub> species. Previous theoretical studies have unveiled that the coupling of two hydrogenated C<sub>1</sub> species is energetically preferred than two \*CO species, since the activation energy for the coupling of two hydrogenated C<sub>1</sub> species is much lower than that of two bare \*CO [86–88]. Dan and coworkers proposed that the formation of adjacently adsorbed \*CH2 and \*CO is of vital importance to guide the reaction selectivity during the CO<sub>2</sub> reduction process to ethanol on Cu-Zn bimetallic systems [42]. To gain further theoretical insight into the conversion of CO2 to ethanol, the \*CH2 and \*CO co-adsorption behavior is simulated on pure Cu (111) and the bimetallic Cu-Zn catalysts. Considering the fact that the incorporation between Cu and Zn results in enhanced CO<sub>2</sub> reduction activity, the co-adsorption behaviors of \*CO and \*CH<sub>2</sub> on neighboring Cu-Zn bimetallic sites are evaluated. In our model, \*CH2 is design to bind with Cu while \*CO binds with Zn, as Cu is believed to lead the reduction of CO<sub>2</sub> to hydrocarbon compounds [89]. As shown in Figs. 5 and S24bond length of 2.422 Å, which is even smaller than that of Cu-Zn. That implies a strong probability for the formation of the new CeC bond. Based on the above discussion, for  $\text{Cu}_5\text{Zn}_8$  catalyst, after forming the intermediate of two coadsorbed \*CO species, one of the adsorbed \*CO species goes through a hydrogenation process, combining with four proton and electron pairs to generate a \*CH2 intermediate. In the next elementary step, the proton and electron pair attacks the other \*CO species to form a \*COH state, which combines with the previously formed \*CH2 to give rise to an adsorbed \*CH2COH intermediate. The \*CH2COH intermediate will thereafter combine with three proton and electron pair to release ethanol eventually.

# 3. Conclusion

To summarize, we demonstrate the catalytic synergies of Cu and Zn to promote  $CO_2$  electroreduction towards liquid  $C_2$  products using hierarchically porous Cu/Zn alloy catalysts. The bimetallic Cu/Zn alloy catalysts prepared through an interfacial self-assembly method allow us to tune the alloy composition by simply varying the ratios of metal precursors. The HMMP

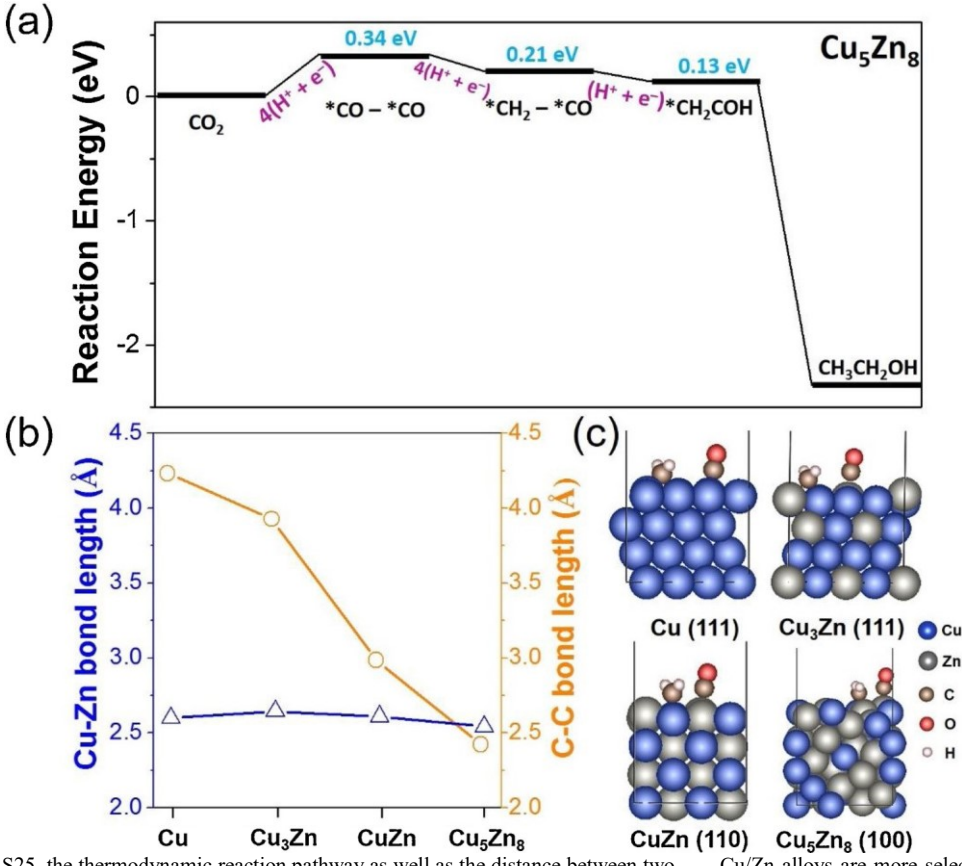


Fig. 5. (a) The calculated reaction energy diagram for the electroreduction of CO<sub>2</sub> to ethanol over the Cu<sub>3</sub>Zn<sub>8</sub> alloy. (b) C-C distance of \*CO and \*CH<sub>2</sub> coadsorption vs. Cu-Zn distance on Cu, Cu<sub>3</sub>Zn, CuZn, and Cu<sub>5</sub>Zn<sub>8</sub>. Noting that in the case of pure Cu, it is the Cu-Cu distance presented. (c) Side view of the most stable configuration of \*CO and \*CH<sub>2</sub> coadsorption on Cu (111), Cu<sub>3</sub>Zn (111), CuZn (110) and Cu<sub>5</sub>Zn<sub>8</sub>(100), respectively.

S25, the thermodynamic reaction pathway as well as the distance between two adsorbed carbon-based intermediates were calculated. The energy toward the bound intermediates \*CO-\*CO (the step with the highest reaction energy) on Cu<sub>5</sub>Zn<sub>8</sub> (100) is lower than that of the pure Cu (111), Cu<sub>3</sub>Zn (111), CuZn (110) catalysis. This confirms that the formation of CeC bonds on Cu<sub>5</sub>Zn<sub>8</sub> is thermodynamically favorable (Figs. 5a and S23). In addition, the distance between the two active binding sites (Cu-Zn distance in bimetallic catalysts) is almost the same among the four catalysts (Figs. 5b and S24); however, the CeC distance of the most stable binding configuration varies significantly depending on the Zn content. On pure Cu (111) surface, the co-adsorbed \*CH<sub>2</sub> and \*CO shows the largest CeC distance of 4.233 Å, indicating a poor tendency for the CeC coupling. When Zn is incorporated to Cu, the CeC distance decreases. On the CuZn (110) surface, the length between the two C<sub>1</sub> species decreases to 2.986 Å suggesting a higher possibility for the CeC coupling (Fig. 5c). Eventually, the two co-adsorbed C<sub>1</sub> species on the surface of Cu<sub>5</sub>Zn<sub>8</sub> shows a

Cu/Zn alloys are more selective for  $CO_2$  reduction, compared to the pure Cu catalyst. A higher Zn content in the HMMP Cu/Zn alloys resulted in weakly adsorbed CO species in higher coverage of the catalysts that simultaneously suppressed the reduction of protons. The HMMP bimetallic Cu/Zn catalysts show a higher selectivity towards the production of  $C_2$  products like ethanol and acetate. For the HMMP  $Cu_5Zn_8$  catalyst at -0.8 V, the FE of ethanol is 46.6 % with a specific current density ( $J_{ethanol}$ ) of 2.3 mA/cm² and the total FE of liquid  $C_2$  products closes to 60 %. The HMMP  $Cu_5Zn_8$  catalyst shows excellent durability and it remains stable to produce ethanol after 11 h electrolysis. Using DFT calculations, the electron-rich Cu in all cases of bimetallic Cu/Zn catalysts showed promoted adsorption of  $CO_2$  and simultaneously suppressed adsorption of  $H_2$ . The tendency of CeC coupling is controlled by the EC content in EC current alloys. The hierarchically porous EC culculated by used for the design of other bimetallic or trimetallic alloys catalysts to reduce EC0 highvalue products. In

view of the long retention time of reduction intermediates closed to the catalysts surface, hierarchically porous Cu-containing catalysts will be of interest to produce hydrocarbon and alcohol from CO<sub>2</sub> electroreduction.

#### Author contributions

B. Liu and J. He conceived the project. X. Su carried out the experiments with the help from L. Jin, L. Zhang, Y. Yang, P. Kerns. Y. Sun and S. Li conducted the theoretical calculations. All authors discussed the results and cowrote the paper.

# **Declaration of Competing Interest**

The authors declare that they have no known competing financial interests or personal relationships that could have appeared to influence the work reported in this paper.

#### Acknowledgments

We thank Professor Gonghu Li and Sebastian A. Pantovich (University of New Hampshire) for the measurement of in situ ATRSEIRAS. J.H. thanks the financial support from the University of Connecticut and the National Science Foundation (CBET #1705566). The SEM/TEM studies were performed using the facilities in the UConn/FEI Center for Advanced Microscopy and Materials Analysis (CAMMA). This work was also partially supported by the Green Emulsions Micelles and Surfactants (GEMS) Center. S.L. thanks the support of the computing resources from National Supercomputing Centre Singapore.

#### Appendix A. Supplementary data

Supplementary material related to this article can be found, in the online version, at doi:https://doi.org/10.1016/j.apcatb.2020.118800.

#### References

- [1] J.-M. Savéant, Chem. Rev. 108 (2008) 2348–2378.
- [2] J. Schneider, H. Jia, J.T. Muckerman, E. Fujita, Chem. Soc. Rev. 41 (2012) 2036–2051.
- [3] E.E. Benson, C.P. Kubiak, A.J. Sathrum, J.M. Smieja, Chem. Soc. Rev. 38 (2009) 89–99.
- [4] Y. Li, Q. Sun, Adv. Energy Mater. 6 (2016) 1600463.
- [5] K.P. Kuhl, E.R. Cave, D.N. Abram, T.F. Jaramillo, Energy Environ. Sci. 5 (2012) 7050–7059.
- [6] Z. Gu, H. Shen, L. Shang, X. Lv, L. Qian, G. Zheng, Small Methods 2 (2018) 1800121.
- [7] K. Hara, A. Kudo, T. Sakata, J. Electroanal. Chem. 391 (1995) 141–147.
- [8] T.T.H. Hoang, S. Ma, J.I. Gold, P.J.A. Kenis, A.A. Gewirth, ACS Catal. 7 (2017) 3313–3321.
- [9] K.D. Yang, W.R. Ko, J.H. Lee, S.J. Kim, H. Lee, M.H. Lee, K.T. Nam, Angew. Chem. Int. Ed. 56 (2017) 796–800.
- [10] S. Sen, D. Liu, G.T.R. Palmore, ACS Catal. 4 (2014) 3091–3095.
- [11] N. Morlanés, K. Takanabe, V. Rodionov, ACS Catal. 6 (2016) 3092-3095.
- [12] D. Raciti, K.J. Livi, C. Wang, Nano Lett. 15 (2015) 6829-6835.
- Y. Li, F. Cui, M.B. Ross, D. Kim, Y. Sun, P. Yang, Nano Lett. 17 (2017) 1312–1317.
   L. Zhang, Z.-J. Zhao, J. Gong, Angew. Chem. Int. Ed. 56 (2017) 11326–11353.
- [15] Y.-X. Duan, F.-L. Meng, K.-H. Liu, S.-S. Yi, S.-J. Li, J.-M. Yan, Q. Jiang, Adv. Mater. 30 (2018) 1706194.
- [16] R. Reske, H. Mistry, F. Behafarid, B. Roldan Cuenya, P. Strasser, J. Am. Chem. Soc. 136 (2014) 6978–6986.
- [17] H. Mistry, A.S. Varela, C.S. Bonifacio, I. Zegkinoglou, I. Sinev, Y.-W. Choi, K. Kisslinger, E.A. Stach, J.C. Yang, P. Strasser, B.R. Cuenya, Nat. Comm. 7 (2016) 12123.
- [18] Z. Ferencz, A. Erdőhelyi, K. Baán, A. Oszkó, L. Óvári, Z. Kónya, C. Papp, H.P. Steinrück, J. Kiss, ACS Catal. 4 (2014) 1205–1218.
- [19] Q. Li, W. Zhu, J. Fu, H. Zhang, G. Wu, S. Sun, Nano Energy 24 (2016) 1–9.
- [20] Y. Huang, A.D. Handoko, P. Hirunsit, B.S. Yeo, ACS Catal. 7 (2017) 1749-1756.
- [21] A. Keskin, M. Gürü, Energy Source A: Recov. Util. Environ. Eff. 33 (2011) 2194-2205.
- [22] Y. Liu, S. Chen, X. Quan, H. Yu, J. Am. Chem. Soc. 137 (2015) 11631-11636.
- [23] A.E. Farrell, R.J. Plevin, B.T. Turner, A.D. Jones, M. Hare, D.M. Kammen, Science 311 (2006) 506.
- [24] J. Hill, E. Nelson, D. Tilman, S. Polasky, D. Tiffany, Proc. Natl. Acad. Sci. U. S. A. 103 (2006) 11206.
- [25] C.W. Lee, K.D. Yang, D.-H. Nam, J.H. Jang, N.H. Cho, S.W. Im, K.T. Nam, Adv. Mater. 30 (2018) 1704717.

- [26] Y. Hori, H. Wakebe, T. Tsukamoto, O. Koga, Electrochim. Acta 39 (1994) 1833-1839.
- [27] H. Yoshio, K. Katsuhei, S. Shin, Chem. Lett. 14 (1985) 1695-1698.
- [28] A.J. Garza, A.T. Bell, M. Head-Gordon, ACS Catal. 8 (2018) 1490-1499.
- [29] D.D. Zhu, J.L. Liu, S.Z. Qiao, Adv. Mater. 28 (2016) 3423-3452.
- [30] I. Merino-Garcia, J. Albo, J. Solla-Gullón, V. Montiel, A. Irabien, J. CO2 Util. 31 (2019) 135–142.
- [31] I. Merino-Garcia, J. Albo, A. Irabien, Nanotechnology 29 (2017) 014001. [32] S. Hanselman, M.T.M. Koper, F. Calle-Vallejo, ACS Energy Lett. 3 (2018) 1062–1067.
- [33] F. Calle-Vallejo, M.T.M. Koper, Angew. Chem. Int. Ed. 125 (2013) 7423-7426.
- [34] D. Ren, Y. Deng, A.D. Handoko, C.S. Chen, S. Malkhandi, B.S. Yeo, ACS Catal. 5 (2015) 2814–2821.
- [35] Y. Jiao, Y. Zheng, P. Chen, M. Jaroniec, S.-Z. Qiao, J. Am. Chem. Soc. 139 (2017) 18093–18100.
- [36] Y. Mi, X. Peng, X. Liu, J. Luo, ACS Appl. Energy Mater. 1 (2018) 5119-5123.
- [37] M. Morimoto, Y. Takatsuji, R. Yamasaki, H. Hashimoto, I. Nakata, T. Sakakura, T. Haruyama, Electrocatalysis 9 (2018) 323–332.
- [38] S. Sarfraz, A.T. Garcia-Esparza, A. Jedidi, L. Cavallo, K. Takanabe, ACS Catal. 6 (2016) 2842–2851.
- [39] D. Kim, J. Resasco, Y. Yu, A.M. Asiri, P. Yang, Nat. Commun. 5 (2014) 4948. [40] H.S. Jeon, I. Sinev, F. Scholten, N.J. Divins, I. Zegkinoglou, L. Pielsticker, B.R. Cuenya, J. Am. Chem. Soc. 140 (2018) 9383–9386.
- [41] D.H. Won, H. Shin, J. Koh, J. Chung, H.S. Lee, H. Kim, S.I. Woo, Angew. Chem. Int. Ed. 55 (2016) 9297–9300.
- [42] D. Ren, B.S.-H. Ang, B.S. Yeo, ACS Catal. 6 (2016) 8239-8247.
- [43] G. Keerthiga, R. Chetty, J. Electroanal. Chem. 164 (2017) H164-H169.
- [44] J. Albo, A. Sáez, J. Solla-Gullón, V. Montiel, A. Irabien, Appl. Catal. B 176–177 (2015) 709–717
- [45] M. Ma, K. Djanashvili, W.A. Smith, Angew. Chem. Int. Ed. 55 (2016) 6680-6684.
- [46] H. Song, M. Im, J.T. Song, J.-A. Lim, B.-S. Kim, Y. Kwon, S. Ryu, J. Oh, Appl. Catal. B 232 (2018) 391–396.
- [47] A. Dutta, M. Rahaman, N.C. Luedi, M. Mohos, P. Broekmann, ACS Catal. 6 (2016) 3804–3814
- [48] A.S. Hall, Y. Yoon, A. Wuttig, Y. Surendranath, J. Am. Chem. Soc. 137 (2015) 14834– 14837
- [49] F. Li, L. Chen, G.P. Knowles, D.R. MacFarlane, J. Zhang, Angew. Chem. Int. Ed. 56 (2017) 505–509.
- [50] J.-J. Lv, M. Jouny, W. Luc, W. Zhu, J.-J. Zhu, F. Jiao, Adv. Mater. 30 (2018) 1803111.
- [51] X. Su, L. Gao, F. Zhou, G. Duan, Sens. Actuators B: Chem. 251 (2017) 74–85.
- [52] Z. Dai, Y. Li, G. Duan, L. Jia, W. Cai, ACS Nano 6 (2012) 6706-6716.
- [53] B. Liu, L. Jin, H. Zheng, H. Yao, Y. Wu, A. Lopes, J. He, ACS Appl. Mater. Interfaces 9 (2017) 1746–1758.
- [54] B. Liu, Z. Luo, A. Federico, W. Song, S.L. Suib, J. He, Chem. Mater. 27 (2015) 6173–6176.
- [55] D. Liu, Q. Lu, Y. Luo, X. Sun, A.M. Asiri, Nanoscale 7 (2015) 15122-15126.
- [56] S.-W. Lee, M.-Y. Huh, E. Fleury, J.-C. Lee, Acta Mater. 54 (2006) 349–355.
- [57] K.-H. Kim, S.-W. Lee, J.-P. Ahn, E. Fleury, Y.-C. Kim, J.-C. Lee, Met. Mater. Int. 13 (2007) 21.
- [58] J. Luo, M. Monai, C. Wang, J.D. Lee, T. DuchoÅ^, F. DvoÅTMák, V. MatolÃn, C.B. Murray, P. Fornasiero, R.J. Gorte, Catal. Sci. Technol. 7 (2017) 1735–1743.
- [59] L. Rout, A. Kumar, R.S. Dhaka, G.N. Reddy, S. Giri, P. Dash, Appl. Catal. A 538 (2017) 107–122.
- [60] G. Yin, H. Abe, R. Kodiyath, S. Ueda, N. Srinivasan, A. Yamaguchi, M. Miyauchi, J. Mater. Chem. A 5 (2017) 12113–12119.
- [61] M. Liu, W. Zhou, T. Wang, D. Wang, L. Liu, J. Ye, Chem. Comm. 52 (2016) 4694–4697.
- [62] D. Chen, P. Sun, H. Liu, J. Yang, J. Mater. Chem. A 5 (2017) 4421–4429.
- [63] Y. Shen, Y. Zhou, D. Wang, X. Wu, J. Li, J. Xi, Adv. Energy Mater. 8 (2018) 1701759.
- [64] B. Hammer, Y. Morikawa, J.K. Nørskov, Phys. Rev. Lett. 76 (1996) 2141-2144.
- [65] M. Wakisaka, S. Mitsui, Y. Hirose, K. Kawashima, H. Uchida, M. Watanabe, J. Phys. Chem. B 110 (2006) 23489–23496.
- [66] O.A. Baturina, Q. Lu, M.A. Padilla, L. Xin, W. Li, A. Serov, K. Artyushkova, P. Atanassov, F. Xu, A. Epshteyn, T. Brintlinger, M. Schuette, G.E. Collins, ACS Cataly. 4 (2014) 3682–3695.
- [67] M. Gattrell, N. Gupta, A. Co, J. Electroanal. Chem. 594 (2006) 1-19.
- [68] Y. Hori, A. Murata, Y. Yoshinami, J. Chem. Soc. Faraday Trans. 87 (1991) 125-128.
- [69] Y. Hori, O. Koga, Y. Watanabe, T. Matsuo, Electrochim. Acta 44 (1998) 1389–1395.
  [70] A. Bard, L. Faulkner, Electrochemical Methods: Fundamentals and Applications, John Wiley & Sons, Inc. 2001.
- [71] B. Hammer, J.K. Nørskov, Surf. Sci. 343 (1995) 211–220.
- [72] Z.W. Ulissi, A.J. Medford, T. Bligaard, J.K. Nørskov, Nat. Commun. 8 (2017) 14621.
  [73] J.K. Nørskov, T. Bligaard, A. Logadottir, J.R. Kitchin, J.G. Chen, S. Pandelov, U. Stimming, J. Electroanal. Chem. 152 (2005) J23.
- [74] E. Andrews, M. Ren, F. Wang, Z. Zhang, P. Sprunger, R. Kurtz, J. Flake, J. Electrochem. Soc. 160 (2013) H841–H846.
- [75] Y. Yang, J. Evans, J.A. Rodriguez, M.G. White, P. Liu, Phys. Chem. Chem. Phys. 12 (2010) 9909–9917.
- [76] J. Albo, M. Perfecto-Irigaray, G. Beobide, A. Irabien, J. CO2 Util. 33 (2019) 157-165.
- [77] J. Rosen, G.S. Hutchings, Q. Lu, R.V. Forest, A. Moore, F. Jiao, ACS Catal. 5 (2015) 4586–4591.

- [78] K. Liu, J. Wang, M. Shi, J. Yan, Q. Jiang, Adv. Energy Mater. 9 (2019) 1900276. [79] T. Zhang, X. Li, Y. Qiu, P. Su, W. Xu, H. Zhong, H. Zhang, J. Catal. 357 (2018) 154–162.
- [80] Y. Hori, H. Wakebe, T. Tsukamoto, O. Koga, Electrochim. Acta 39 (1994) 1833–1839.
- [81] T. Zhang, H. Zhong, Y. Qiu, X. Li, H. Zhang, J. Mater. Chem. A 4 (2016) 16670–16676.
- [82] B. Qin, Y. Li, H. Fu, H. Wang, S. Chen, Z. Liu, F. Peng, ACS Appl. Mater. Interfaces 10 (2018) 20530–20539.
- [83] M. Morimoto, Y. Takatsuji, K. Hirata, T. Fukuma, T. Ohno, T. Sakakura, T. Haruyama, Electrochim. Acta 290 (2018) 255–261.
- [84] W. Luo, J. Zhang, M. Li, A. Züttel, ACS Catal. 9 (2019) 3783-3791.
- [85] S. Lee, G. Park, J. Lee, ACS Catal. 7 (2017) 8594-8604.
- [86] X. Nie, M.R. Esopi, M.J. Janik, A. Asthagiri, Angew. Chem. Int. Ed. 52 (2013) 2459–2462.
- [87] W. Luo, X. Nie, M.J. Janik, A. Asthagiri, ACS Catal. 6 (2016) 219-229.
- [88] J.H. Montoya, A.A. Peterson, J.K. Nørskov, ChemCatChem 5 (2013) 737-742.
- [89] A.A. Peterson, F. Abild-Pedersen, F. Studt, J. Rossmeisl, J.K. Nørskov, Energy Environ. Sci. 3 (2010) 1311–1315.